Multiscale Petrophysical Characterization and Flow Unit Classification of the Minnelusa Eolian Sandstones

Heng Wang[a,b], Zuhao Kou[c,*], Davin A. Bagdonas[b], Erin H.W. Phillips[b], Vladimir Alvarado[c,*], Andrew Charles Johnson[d], Zunsheng Jiao[b], J. Fred McLaughlin[b], Scott Austin Quillinan[b]

[a] *State Key Laboratory of Oil and Gas Reservoir Geology and Exploitation, Chengdu University of Technology, Chengdu 610059, China*
[b] *Center for Economic Geology, University of Wyoming, 1000 E. University Avenue, Laramie, WY, USA, 82071*
[c] *Department of Chemical Engineering, University of Wyoming, 1000 E. University Avenue, Laramie, WY, USA, 82071*
[d] *Schlumberger Digital and Integration, 1675 Broadway St., Suite 900, Denver, Colorado, 80202*

Abstract

Integration of petrophysical and geological information is critical to simulation of subsurface carbon storage (GCS). In this sense, two depositional facies were identified from the core description and well-log interpretation, namely massive (MS) and cross-bedded (CB) facies groups. Additionally, pore-scale characteristics were studied by a combination of techniques, e.g. Nuclear Magnetic Resonance (NMR) and mercury intrusion capillary pressure (MICP). Scanning electron microscope (SEM) and petrographic analyses show that the pore structure is dominantly controlled by the depositional environment and dolomite cementation. NMR-T_2 distributions of MS and CB facies show triple and quadruple modes, respectively. In addition, MICP of high- and low-permeability MS facies samples, and their CB facies group mixtures were collected. The MS sample pore-throat size distribution is uni-modal, while the triple-modal characteristic of the mixtures indicates heterogeneous pore structures at the sub-core scale for CB facies. The reliably estimates of porosity and permeability for both facies groups via NMR techniques and the MLR (Multiple Linear Regression) approach demonstrate the applicability of these techniques to eolian sandstone. Moreover, irreducible water saturation via the T_2-cutoff method cor-

*Corresponding author
Email addresses: zkou@uwyo.edu (Zuhao Kou), valvarad@uwyo.edu (Vladimir Alvarado)

relates strongly with T_{2LM} instead of porosity. Finally, the rock quality index and flow zone indicator were calculated based on Combinable Magnetic Resonance (CMR) log interpretations. This provides direct connection to properties measured in the well. Four flow units were classified for both facies groups. Results show that better reservoir quality with significant heterogeneities is observed in the CB facies. This study highlights the importance integrating multiscale petrophysical properties including facies, pore architecture and diagenesis analysis with core- to log-scale property characterization. The results herein validate our reservoir characterization and flow unit classification in eolian reservoirs.

Keywords: Geological carbon storage, Eolian sandstone, Multiscale petrophysical characterization, Nuclear Magnetic Resonance, Flow unit classification

2010 MSC: 00-01, 99-00

1. Introduction

Wyoming holds more than one-third of U.S. coal reserves at producing mines, accounting for about two-fifths of all coal mined in the United States in 2018 (U.S. Energy Information Administration, 2020). Coal mined in the Powder River Basin (PRB) located in northeastern Wyoming, is mainly used at power plants. Large quantities of carbon dioxide (CO_2) emissions from coal power plants contribute to the rising atmospheric CO_2 concentration and thus to climate change (IPCC, 2013). Therefore, substantial and sustained reduction of greenhouse gas emissions, especially CO_2, are required if thermal coal is to remain relevant as a fuel in electricity generation. Geologic Carbon Storage (GCS) has been extensively explored as a feasible technology in recent years (Saghafi et al., 2007; Godec et al., 2013; Gong and Gu, 2015; Jiang et al., 2019; Zhang et al., 2019; Yu et al., 2021). The Dry Fork Station (DFS) storage complex located in the PRB was selected to evaluate the potential for CO_2 storage, including assessment of storage capacity, reservoir petrophysical properties, and

the sealing capacity of the cap rocks. A stratigraphic well (the UWPRB#1) was drilled near the Dry Fork Station and the primary studies identified the Lakota Formation, the Hulett Member of the Lower Sundance Formation, and the Upper Minnelusa Formation as potential reservoirs to satisfy CO_2 volumetric storage requirements of the Carbon Storage Assurance Facility Enterprise (CarbonSAFE) project.

As one of the main storage targets, the eolian Minnelusa Sandstone reservoirs in the PRB comprise a series of stacked dunes, interdunes, and sand sheets, resulting in drastic variations within sedimentary lithofacies in a short vertical and lateral range (Jorgensen and James, 1988; Chandler et al., 1989). In addition, the very fine sand deposited within the same facies, such as stacked dunes, also introduce heterogeneities at multiple scales, starting at the sub-core down to the pore cale. For instance, the high-angle avalanche beds are separated by the typically finer grained grainfall sediments, which often become permeability barriers within the sand sequence. Diagenesis is another important factor influencing heterogeneities, which is a function of depositional environment, cement precipitation and dissolution, sand composition, and burial history, and can dramatically alter the pore structure (Krystinik, 1990; Schenk, 1990; Kou et al., 2021). Many eolian deposits with consistent mineralogy and good porosity development were intensely cemented by anhydrite and/or dolomite. The multi-length-scale heterogeneity of petrophysical properties and their spatial distribution can translate into distinct characteristics of the subsurface fluid-rock system such as pore architecture, porosity, permeability, and irreducible water saturation or a combination of these. These petrophysical characteristics negatively impact CO_2 injectivity, flow regimes, migration, and storage capacity, thus raising significant uncertainties in GCS projects (Krevor et al., 2011; Al-Bayati et al., 2019; Liu et al., 2019; Chen et al., 2021; Han et al., 2021).

As the CO_2 injectivity, flow regimes, trapping mechanisms, migration, and storage capacity vary with rock types, especially for eolian sandstones, reservoir rocks classification is necessary for geological modeling and reservoir simulation for GCS (Padhi et al., 2014; Wei et al., 2014; Singh, 2018; Al-Bayati et al., 2019;

Newell et al., 2019; Zheng et al., 2021). Rock typing consists of classifying distinct units of reservoir rocks by employing lithofacies, petrophysical rock/pore properties, rock-fluid interactions, and/or historic production/injection performances (Gunter et al., 1997; Guo et al., 2007; Rebelle and Lalanne, 2014). Several clustering methods can be used in reservoir characterization (Rebelle and Lalanne, 2014): 1) geology driven clustering, 2) porosity-permeability driven clustering, 3) cut-off based clustering, 4) capillary pressure driven clustering, 5) logs driven clustering, and 6) dynamic driven clustering methods. Currently, rock-typing studies more likely rely on linking two or more clustering methods (Salman and Bellah, 2009; Rebelle et al., 2009; Skalinski and Kenter, 2015; Chandra et al., 2015; Farshi et al., 2019). However, as opposed to oil/gas reservoirs, where abundant data have been collected during exploration and development stages, available data for deep saline aquifers for GCS are limited.

The objectives of this study are: (1) multiscale petrophysical properties characterization and (2) classification of flow units of the Minnelusa eolian sandstones at the UWPRB#1. These objectives depend on characterization and analysis tasks. In this sense, links between pore-scale characteristics with core-scale properties, i.e. porosity, permeability and the irreducible water saturation were investigated. Then these petrophysical properties interpreted from well-log data were analyzed. Finally, reservoir quality index (RQI) and flow zone indicator (FZI) were calculated using data interpreted from Schlumberger Combinable Magnetic Resonance (CMR) log, and the discrete rock types (DRT) were classified as the flow units, which can be employed in the 3D geological modeling and reservoir simulation of CO_2 injection in the eolian units. Results in this study also provide a comprehensive understanding of petrophysical properties in multiscale and flow capacity of different flow units in the eolian Minnelusa Sandstones to provide a better reference for field operations.

2. Geological settings

The Powder River Basin (PRB), as shown in Fig. 1, is located in northeastern Wyoming and southeastern Montana. The basin, developed during the Laramide Orogenic tectonic shortening, is asymmetric with the synoformal axis oriented approximately north-south along the western third of the structure. Basin bounding features including the Black Hills and Hartville Uplift on the east, Laramie Range and Casper Arch to the south, Bighorn Mountains, and the Hardin Platform on the west, and the Miles City arch, Bull Mountains, and Porcupine dome on the north were shown (Anna, 2009). The Upper Minnelusa formation at the Dry Fork Station (DFS) storage complex, located in the upper-right quadrant of the State and in the region where the UWPRB #1 test well was drilled, consists of varying interbedded marine dolomites and eolian sandstones deposited during several cycles of transgression and regression in Permo-Pennsylvanian time (George, 1984; Jorgensen and James, 1988). Each cycle was terminated by a rapidly rising sea level that deposited carbonates and evaporites of the next cycle (George, 1984). The sandstone intervals of the upper Minnelusa sandstones are commonly labeled alphabetically (Fig. 1), but do not always correlate across the basin entirely. At the UWPRB#1 test well Minnelusa B, C and D sandstones are recognized.

Near DFS, the upper Minnelusa sandstone intervals contain the best reservoir intervals (with the highest porosity and permeability) and can be productive hydrocarbon reservoirs, and dispersed fields exist across much of the eastern margin of the basin (Anna, 2009). Porosity evolution of the Minnelusa sandstones is largely a function of depositional environment, early anhydrite cementation, burial compaction, and later anhydrite dissolution, as well as quartz and dolomite cementation. Minor diagenetic alterations, such as illite and pyrite growth, multigenerational feldspar and dolomite dissolution and growth, and modifications of early clay grain coatings do not significantly add to the evolution of porosity (Schenk, 1990). Permeability of the eolian sandstone complex is highly impacted by stratigraphic architecture and cementation, which could

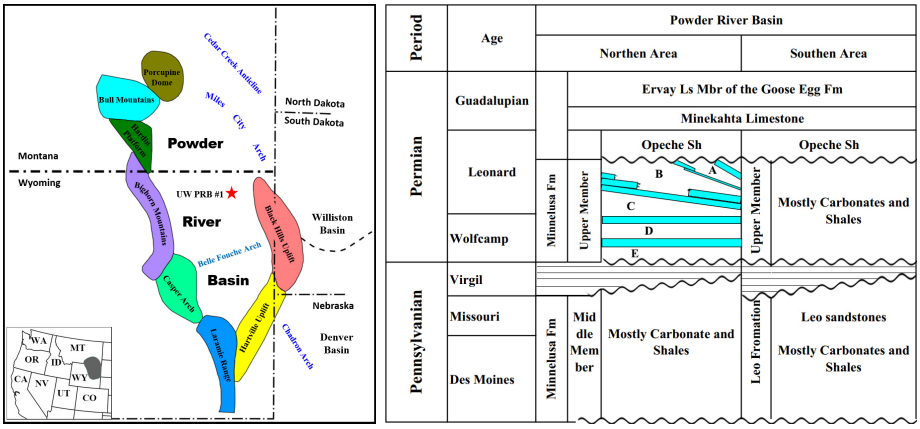

Fig. 1. Left: Generalized diagram showing major structural elements that border the Powder River Basin (PRB). Modified from Shurr et al. (1994) and Anna (2009). Red star shows the location of the UWPRB#1 test well. DFS is located in the northeastern quadrant of the State and in the PRB basin region where the UWPRB #1 test well was drilled. Right: Generalized stratigraphic column of the Minnelusa Formation at PRB. Modified based on Anna (2009).

yield a range of values several orders of magnitude between or within distinct facies, such as dune, interdune and/or sabkha deposits. The lateral and vertical stacking of eolian and sabkha deposits lead to the heterogeneity of permeability at the macroscale. In addition, the direction of the greatest permeability is usually perpendicular to the wind direction of dune-face formation and parallel to the long axis of the dune within bedding sets. At the microscale, a change in grain size at the base of the dune and cementation due to capillary action and evaporation of sulphate and calcium rich fluids can create potential barriers within the dune complex, which further leads to the complex permeability distributions. These natural barriers are reflected in Minnelusa oil fields, which commonly exhibit a limited water drive, being indicative of confinement from surface and other reservoirs (Anna, 2009). However, as a storage system, it provides attractive qualities for potential GCS reservoir consideration. The regionally extended caprock of the upper Minnelusa Formation is the Permian Opeche Shale, which serves as a regionally extensive confining layer. Moreover, the lower cycles of the upper Minnelusa sandstones within the study area are confined by carbonates, which are most often sealing. Finally, the Dry Fork

Station is located close to the UWPRB#1 test well and provides a CO_2 emission source, which makes the storage complex in the PRB a suitable candidate for commercial carbon dioxide capture and storage.

3. Materials and methods

3.1. Materials

Synthetic or surrogate brines used to saturate core plugs were prepared following the composition shown in Table 1. Down-hole formation brine samples from the Minnelusa B, C and D sandstones provided the basis for the synthetic brines. All brines were prepared in the laboratory by dissolving specified amounts of analytic-grade salts in deionized water. After mixing, brines were filtered and degassed under vacuum before use. Rock plugs (38.1 mm in diameter) of the Minnelusa formation were drilled from core samples recovered from the UWPRB#1. Core samples were cleaned in soxhlet extractors using toluene and methanol, and oven-dried at 100 °C for 24 hours.

Table 1: Chemical concentrations, total dissolved solids (TDS) and pH of synthesized brines (Unit: mg/kg).

Major Species	Minnelusa B	Minnelusa C	Minnelusa D
SO_4	5,060	4,370	5,745
HCO_3	920	810	945
Cl	54,700	32,400	56,300
K	3,960	1,820	4,080
Na	35,600	20,800	34,050
Mg	58	92	32
Ca	1,140	757	1,140
TDS	101,445	61,056	102,299
pH	7.25	6.7	6.67

3.2. Experimental methods

Routine core porosity and permeability measured using nitrogen at a net confining pressure of 6.9 MPa (1000 psi) were carried out using a Coreval 700 porosimeter and permeameter (VINCI Technologies, France). Properties of each

sample are summarized in Table 2. Samples prepared for the thin section were trimmed from the core plug ends and pore structures were determined by thin section analyses and revealed by blue-dyed epoxy. Small rock pieces from the trimmed parts were carbon-coated for SEM imaging.

Table 2: Summary of properties of core plugs measured in the laboratory. Porosity and permeability were measured under a net confining pressure of 6.9 MPa.

Sample ID	Depth ft	ϕ_{lab} fraction	k_{lab} mD	T_{2LM} ms	k_{SDR} mD	k_{TC} mD	S_{wir} fraction
MH1	9,382.4	0.053	0.747	41.7	0.111	0.618	0.022
MH2	9,388.6	0.092	4.466	44.9	1.150	6.469	0.019
MH3	9,398.0	0.071	1.311	43.3	0.380	2.384	0.019
MH4	9,444.6	0.068	0.494	43.8	0.298	0.072	0.254
MH5	9,451.2	0.078	0.893	56.5	0.832	0.941	0.042
MH6	9,460.3	0.063	6.243	73.2	0.647	1.845	0.014
MH7	9,463.8	0.112	38.914	175.4	37.628	8.315	0.002
MH8	9,464.2	0.084	9.047	65.3	1.651	1.539	0.025
MH9	9,464.5	0.065	0.613	43.8	0.270	0.993	0.031
MH10	9,470.2	0.090	2.512	75.1	2.929	9.063	0.013
MH11	9,475.6	0.042	0.044	10.7	0.003	0.006	0.392
MH12	9,486.6	0.081	2.326	87.7	2.355	2.823	0.017
MH13	9,493.8	0.082	8.708	89.8	2.582	4.234	0.012
MH14	9,499.3	0.045	0.070	57.6	24.10	0.218	0.021
MH15	9,505.3	0.052	0.051	28.0	0.041	0.018	0.317
MH16	9,511.0	0.050	0.073	26.1	0.029	0.024	0.219
MH17	9,535.3	0.101	20.856	187.5	25.786	17.985	0.006
MH18	9,538.8	0.136	84.266	168.4	76.610	81.618	0.007

ϕ_{lab}: Lab gas porosity; k_{lab}: gas-corrected absolute permeability; T_{2LM}: Transverse relaxation time log-average; k_{SDR}: absolute permeability calculated based on SchlumbergerDoll Research (SDR) correlation; k_{TC}: absolute permeability calculated based on the Timur-Coates model; S_{wir}: irreducible water saturation from T_2 spectra.

Samples from the MS facies group, high- and low-permeability, and their mixtures from the CB facies group were cut adjacent to the core plugs for MICP measurement. The experiment was conducted at Core Laboratories Petro Services (Denver, CO) using an AutoPore V instrument (Micromeritics Instrument Corporation). Distribution of pore-throat radius can be obtained from the MICP curves as:

$$r = -\frac{2\sigma cos\theta}{Pc(S_{Hg})} \tag{1}$$

where σ, the interfacieal tension of the mercury/air is 0.48 N/m, Pc is capillary pressure, θ, contact angle of mercury/air commonly equals 140°, S_{Hg} is the mercury saturation.

Proton nuclear magnetic resonance (^{1}H NMR) T_2 relaxation time, also known as transverse relaxation time, was used to estimate the pore-size distribution. T_2 relaxation mechanisms are described in our previous publication (Wang et al., 2018). In addition, NMR T_2 spectra have been frequently used for permeability estimation in both laboratory and well logging (Kenyon, 1997; Coates et al., 1999; Alvarado et al., 2003; Ren et al., 2019) as pore-throat size is believed to correlate strongly with pore-body size for most sandstone. Two of the most commonly used models for permeability estimation are the semiempirical SchlumbergerDoll Research (SDR) and the Timur-Coates (TC) or free fluid model. The SDR model is based on Kenyon relationship (Kenyon et al., 1988; Kenyon, 1992) using measurements of sandstone permeability (k), porosity (ϕ), and the logarithm mean value of the T_2 distribution (T_{2LM}), as expressed in Equation 2. Coates et al. (1991) developed the Timur-Coates model based on the bound-fluid porosity (BFI) and the free fluid porosity (FFI), shown in Equation 3.

$$k_{SDR} = C_1\phi^4 T_{2LM}^2 \tag{2}$$

$$k_{TC} = C_2\phi^4 \left[\frac{FFI}{BFI}\right]^2 \tag{3}$$

where C_1 and C_2 are empirical coefficients; ϕ is fractional porosity; k_{SDR} and k_{TC} are in mD.

3.3. Well-log data

Wireline logs such as gamma ray, spontaneous potential, sonic transit time, neutron and density, were collected in the UWPRB#1. Porosity interpreted

by regressing commonly used log variables, i.e. Density log (RHOZ), Thermal Neutron log (NPHI) and Sonic log (DTCO) from UWPRB #1 well against core-measured values using the multi-linear regression (MLR) approach was also studied. Here, porosity is expressed as: $\phi_{MLR} = a_1 RHOZ + a_2 NPHI + a_3 DTCO + a_0$, where a_0 to a_3 are fitting parameters. For the MLR approach, the core and log data were employed as input parameters for each facies group, and the Least Absolute Shrinkage and Selection Operator, or LASSO regression analysis method was employed. The loss function (L1-norm) was used to minimize the sum of the absolute values of the model coefficients between the measured and predicted results by the linear approximation. In addition, the CMR log was also acquired using Schlumberger's CMR-Plus well logging tool. Primary outputs include transverse relaxation time (T_2) distribution, the logarithmic mean value of T_2, total matrix-independent porosity, free and bound-fluid porosity. The output results allow permeability calculation using the SDR and TC models, eliminating the need for physical samples.

3.4. Fluid unit classification

Many methods that consider petrophysical attributes are commonly used for core-based hydraulic rock typing, such as Reservoir Quality Index (RQI) (Leverett, 1941), Winlands R35 (Pittman, 1992), and Flow Zone Indicator (FZI) (Amaefule et al., 1993). Among these methods, the FZI technique has been successfully used in many studies to characterize hydraulic units (Amaefule et al., 1993; Guo et al., 2007; Gunter et al., 1997). The technique is based on a modified Kozeny-Carmen equation and the concept of mean hydraulic radius. The reservoir quality index (RQI) and the normalized porosity index (ϕ_z) were calculated based on Equation 4, while the FZI was estimated by Equation 5.

$$\begin{aligned} \phi_z &= \frac{\phi_e}{1-\phi_e} \\ RQI &= 0.0314\sqrt{\frac{k}{\phi_e}} \end{aligned} \tag{4}$$

$$FZI = \frac{RQI}{\phi_z} \tag{5}$$

where k is permeability, mD, ϕ_e is the effective porosity, fraction. The effective porosity in this study was obtained from the free fluid porosity (FFI), and permeability was calculated from the SDR model.

The Discrete Rock Type (DRT) that is often employed in geological modeling and reservoir simulation was calculated using Equation 6.

$$DRT = Round(2ln(FZI) + 10.6) \tag{6}$$

4. Results and discussion

4.1. Depositional features and facies classification

The eolian sandstones are composed of three units at UWPRB#1: Minnelusa B, C and D (Fig. 2), which were identified from the well-logs and core descriptions. The yellow fields enveloped between the neutron and density porosity curves together with the help of core description identify the sandstones. In view of the limitations of core descriptions lacking extent enough to adequately describe the lithofacies subgroups of upper Minnelusa reliably, massive, laminar-bedded, and cross-bedded stratigraphy are utilized. Laminar-bedded and cross-bedded differences may not be discernable at a scale relevant to this investigation. Therefore, in this study, laminar- and cross-bedded are grouped as cross-bedded facies group (group 2), and the remaining massive stratigraphy is characterized as massive facies group (group 1), shown in Fig. 2.

Stratigraphic features within the studied depth interval were identified with the help of a 190-ft core recovered from well UWPRB#1. The Minnelusa B unit lies at the top of the upper Minnelusa formation in this core. A 20-ft massive sandstone, including hydrocarbon and transition zones, was found on top of the Minnelusa B sandstone (Min B Ss), but is not the focus of this study. The lower part of the Min B Ss is mainly comprised of a mottled dolomitic massive facies (Facies group 2), which is 5-ft thick. Buff to pink fine-grained to very

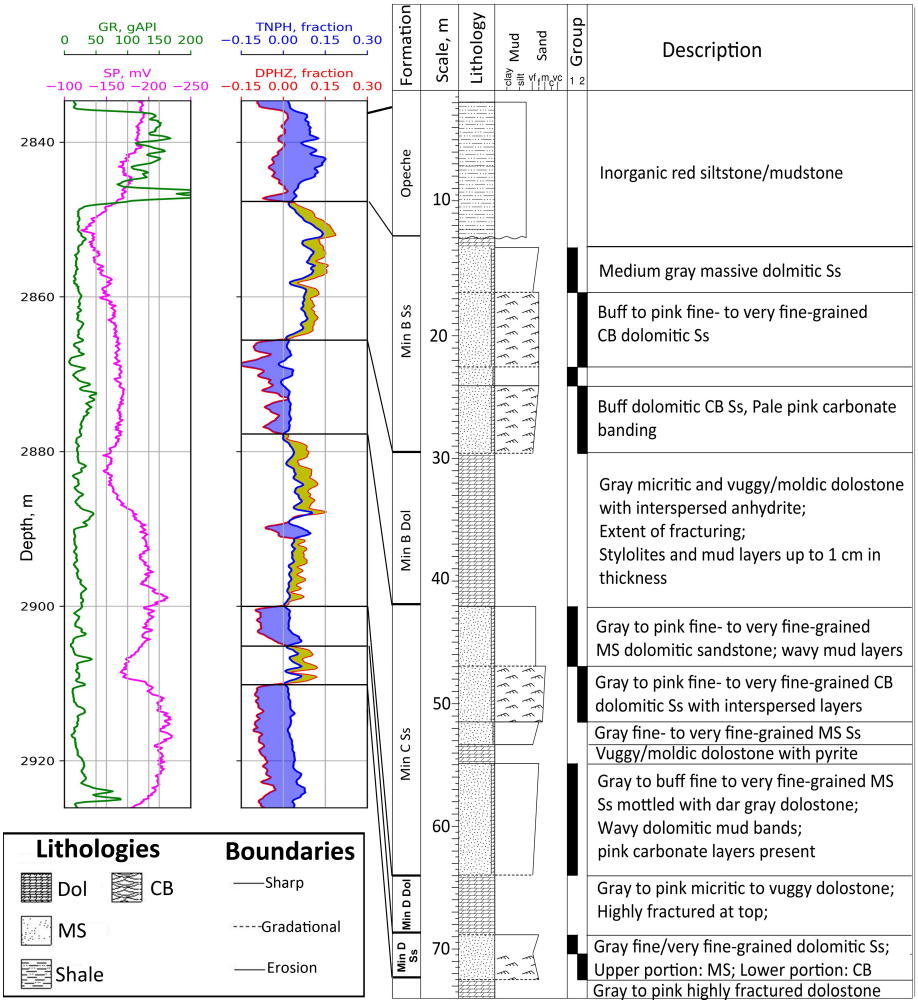

Fig. 2. Well log data and core description results on the well UWPRB#1. On the basis of well log interpretation and core descriptions, Minnelusa B, C and D sandstones were identified, and massive facies and cross-bedded facies groups were separated. GR: Gamma ray; SP: Spontaneous potential; TNPH: Thermal neutron log porosity; DPHZ: Density porosity. Note: the yellow areas between DPHZ and TNPH indicate the sandstone.

fine-grained cross-bedded dolomitic sandstone are observed and portions are very faintly bedded to massive. Figs. 3A and B are cross-bedded and laminar facies from the Minnelua B sandstone, which contain ripple-produced strata. The wind-ripple facies has thin, laminated, millimeter-scale, pin stripe beds. The set of inversely graded strata comprises secondary porosity after dolomite dissolution. An interesting aspect of the core in Fig. 3A is the presence of the 'V' marker above, which is thin, cross-bedded, millimeter-scale sand sheet facies.

The Minnelusa C unit comprises cross-bedded and massive facies groups, and a 6-ft thick dolostone. The massive facies groups on top and in the middle of the Minnelusa C unit depict gray to pink fine-grained to very fine-grained massive dolomitic sandstone with multiple wavy mud layers (Fig. 3E) . While for the massive group on the bottom of the Minnelusa C unit, gray to buff fine-grained to very fine-grained massive dolomitic sandstone mottled with dark gray dolostone was observed. The dark-gray, very fine grained mottling is dolomitic and made visible by diagentic alteration. In addition, it contains wavy dolomitic mud bands and pink carbonate layers up to 10 cm thick are present in lower portion. The cross-bedded facies group located in the middle of the Minnelusa C unit presents gray to pink fine-grained to very fine-grained cross-bedded dolomitic sandstone with interspersed medium-grained layers. Fig. 3D consists of stacks of flat fine laminae, which might be deposited at interdune or sand sheet. Differentiating inter-dune from sand sheet deposits based on sedimentary structure alone is hard in the Minnelusa, as structures are similar in these two facies in modern environment (Fryberger, 1984).

Compared to units B and C, the thickness of the Minnelusa D sandstone is only 17 ft. It presents gray fine-grained to very fine-grained dolomitic sandstone. The massive facies group is located on the upper portion with a thin dolostone layer base, while the lower portion is cross-bedded facies group, shown in Fig. 2. Figs. 3G and H show examples of the upper massive and the lower cross-bedded facies groups. The cross-bedded facies group of the D unit mainly comprises sand sheet produced strata.

Carbonate cycles including A, B, C and D dolomites at UW PRB#1 (ex-

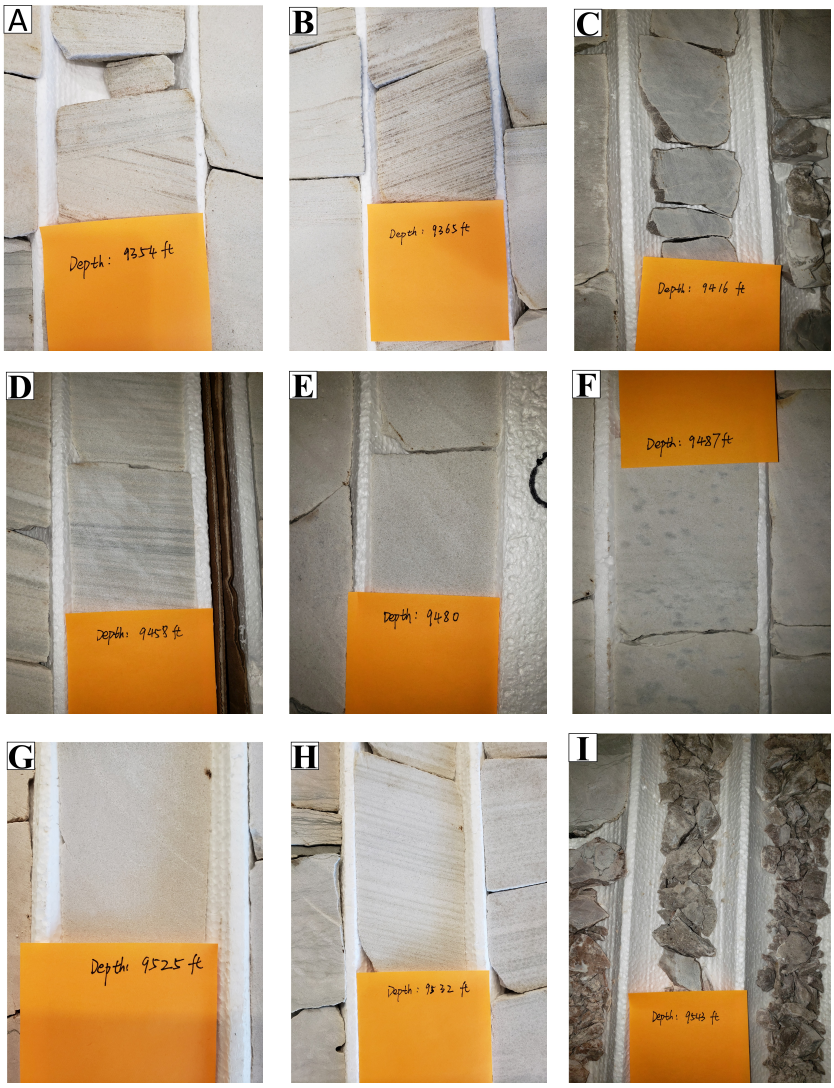

Fig. 3. Examples of the Minnelusa formation facies pictured from the well UWPRB#1. A and B: cross-bedded and laminated facies from the Minnelua B sandstone. Wind-ripple-produced strata. Note above the 'V' marker in A is possibly sand sheet-produced strata; C is from Minnelusa B dolostone; D, E and F show the laminated, massive and mottled massive facies groups, respectively from the Minnelusa C sandstone. D: Sand sheet or interdune deposits with lower angle. F: The dark-gray, very fine grained mottles are dolomitic with the mottling made visible by diagentic alteration; G and H show the upper massive and the lower cross-bedded facies; I shows the highly fractured micritic dolostone from Minnelusa D dolostone. Note: the depth shown on the marker is a 6-ft offset compared with log depth.

amples are shown in Figs. 3C and I) deposited as the water table began to rise in low areas between the dunes during the regression time. The Minnelusa A dolomite overlies on the top of the Minnelusa B sand and is very thin. Minnelusa B dolomite has gray micritic and vuggy/moldic dolostone with interspersed anhydrite. Portions of the dolostone are recrystallized and the extent of fracturing varies throughout the member. Moreover, stylolites and mud layers up to 1 cm in thickness are present. Similar to the B dolomite, the Minnelusa C dolomite also shows gray to pink micritic to vuggy/moldic dolostone. The top portions of the C dolomite and most of the Minnelusa D dolomite were highly fractured micritic dolostone, shown in Figs. 3F and H. Even though the C and D dolomites were fractured, the large salinity differences shown in Table 1 indicate that they are sealed at the well-site.

4.2. Pore structure characterization

4.2.1. SEM and thin section analysis

SEM analysis of rock samples from the Minnelusa reservoir intervals was utilized to unveil pore architecture and understand mineral constituents as they occur in pore and pore-throat volumes from different facies. The samples from core plugs MH6 and MH13, shown in Figs. 4A and B, were used for this comparison. Fig. 4A from the Minnelusa C sand is variably laminar and massive bedded from dune face and interdune input, showing a variety of grain-size distributions (average size from <30 μm to >400 μm) resulting in pore-size variability. Both microcrystalline dolomite and anhydrite occur as cements with lenticular nodules being associated with bedding strata. Fig. 4B shows an SEM image of core sample MH13, which is distinctive of massive bedded interdune material of relatively homogeneous grain-size resulting in similar pore size. It exhibits prevalent microcrystalline dolomite cementation, which is the primary mineral after quartz in this sample. Cement often occurs as nodules with intergranular texture and associated carbonate-bound secondary pore networks throughout the sample and is apparently not associated with bedding like Sample MH6.

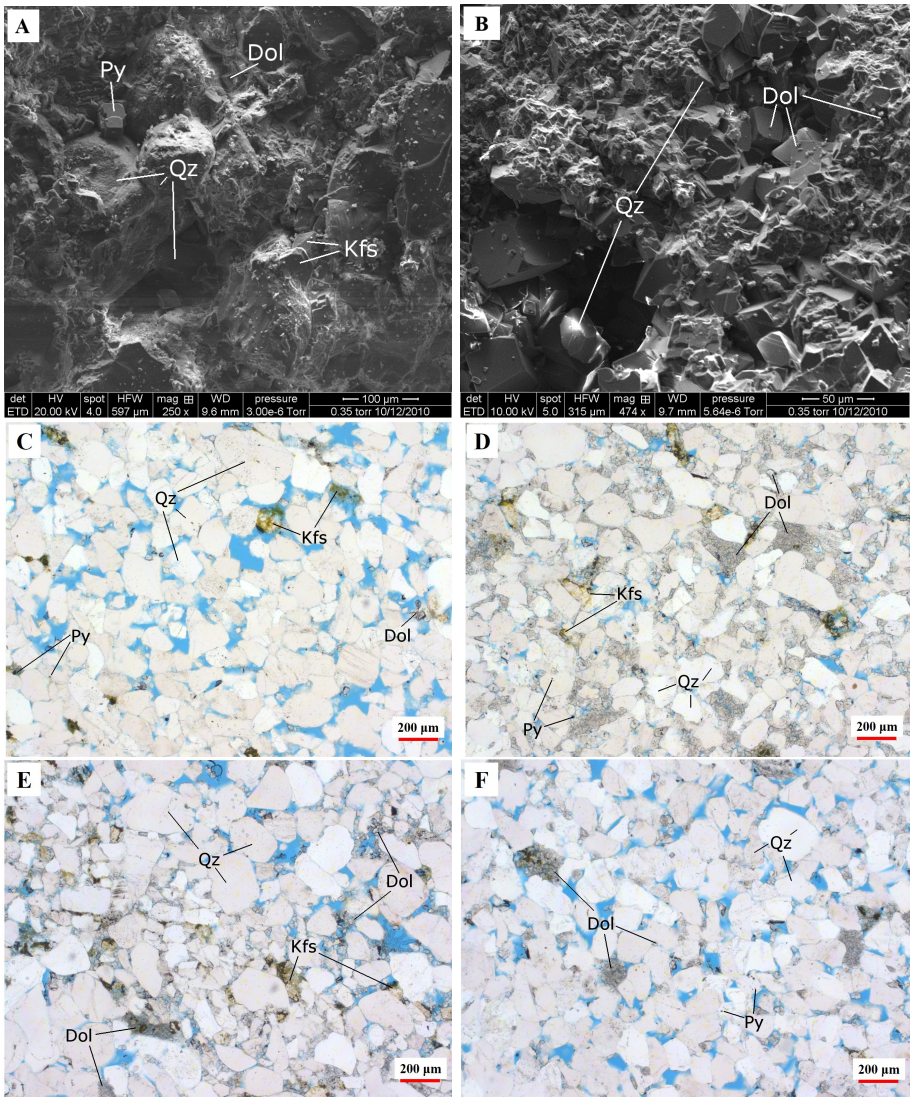

Fig. 4. SEM and thin section images of cross-bedded (A, C and E) and massive (B, D and F) facies group samples, respectively. A, C and E were collected from MH6, MH6 and MH7, respectively; B, D and F were collected from MH13, MH13 and MH17, respectively. Dolmite, pyrite and K-feldspar were observed for both facies groups. For the CB facies group, the size of pores are more homogeneous in high permeable layers (C), while they are more heterogeneous in the lower permeable layers (E). For the MS facies group (D and F), porosity is mainly controlled by the pore-filling dolomite cement, which often occurs as nodules. Qz: Quartz, Dol: Dolomite, Py: Pyrite, Kfs: K-feldspar.

Thin section analysis was used to describe the stratigraphic type, pore structure, and mineralogy of Minnelusa sands collected from UWPRB#1. From thin section-scale analysis, three primary stratigraphy types emerged. These are massive-bedded (with variable sorting), laminar-bedded (with moderate sorting and variable cementation), and cross-bedded moderately sorted (with variable cementation). Laminar-bedded samples may be cross-bedded or horizontally deposited interdune material depending on location in the dune field deposition environment. Figs. 4C-F show examples of the four thin sections derived strata descriptions, and the sample identification are as follows.

Sample MH6 (Cross-bedded, Fig. 4C): Moderately to poorly sorted, sub-rounded to rounded, quartz dominated, with average grain size ranging from <30 to >400 μm. This sample exhibits both matrix and grain supported areas, though grain supported matrix is dominant. Microcrystalline dolomite cement and anhydrite cement are prevalent and are the primary mineral after quartz in this sample, often occurring in nodules. Anhydrite tends to occur in lenticular nodules associated with bedding. The largest primary grains tend to be rounded to well-rounded with finer grain materials being more angular in character. Potassium feldspar occurring 5% - 10% of the mineralogy is present, mostly as a secondary mineral, though relic grains do exist. Opaque minerals occur within the majority of microcrystalline dolomite cements, which occupy most pore space edges, though not all pores are cemented. Dolomite cements where no associated with nodules tend to be grain surface coatings with open pore space remaining between most quartz grains.

Sample MH7 (Laminar-bedded, Fig. 4E): Laminar bedded, moderately to poorly sorted, sub-rounded to rounded, quartz dominated. Bedding is defined by depositional grain packing rather than grain size. Primary grains range from <40 to >420 μm (though other intervals of this facies have grain sizes ranging from <40 to >300 μm). This sample exhibits both matrix and grain supported areas, though grain supported matrix is dominant. Microcrystalline dolomite cement is the most abundant mineral after quartz in this sample, often occurring in clusters and grain coatings. Anhydrite tends to occur in lenticular

nodules associated with bedding. The largest primary quartz grains tend to be rounded to well-rounded with finer grain materials being more angular in character. Potassium feldspar occurring 5-10% of the mineralogy is dominantly as a secondary mineral, though relic grains do exist. Opaque minerals occur within the majority of microcrystalline dolomite cements, which occupy most pore space edges, though not all pores are cemented.

Sample MH13 (Massive-bedded, Fig. 4D) is a well sorted, sub-rounded to rounded, grain supported, quartz sandstone. Primary grains with average size range from <50 to >140 μm with rare larger grains occurring up to 220 μm in diameter. Micro-crystalline dolomite cement is prevalent and is the primary mineral after quartz in this sample, often occurring as nodules with intergranular texture and associated secondary pore networks, and as grain coatings distributed throughout the pore network. Potassium feldspar occurring less than 5% of the mineralogy is dominantly as a secondary mineral, occurring as grain coatings along pore boundaries, though relic grains do exist. Opaque minerals occur within the majority of microcrystalline dolomite cements, which occupy most pore space edges. Minor anhydrite cement is present in a few pores.

Sample MH17 (Massive-bedded, Fig. 4F) is a moderately well sorted, sub-angular to sub-rounded, grain supported, quartz, with average size ranging from <50 to >160 μm. Apparent porosity is very good compared to sample MH13. Microcrystalline dolomite cement is present in small amounts, occurring as nodules with intergranular texture with associated secondary pore networks, and as single grains adhered to quartz grain boundaries. Potassium feldspar makes up approximately 3% to 5% of the mineralogy and is dominantly as a secondary mineral occurring as grain coatings along pore boundaries, though relic grains do exist. Opaque minerals make up less than 1% of the rock and most often occur with potassium feldspar.

The above descriptions indicate that the differences between laminar- and cross-bedded lithologies from thin section descriptions are too small to be considered different. Grain sorting, grain size variability with exception of a few larger grains, cementation occurrence, and secondary mineral occurrence are all simi-

lar. In contrast, the difference between bedded (laminar- and/or cross-bedded) and massive Minnelusa facies is obvious from thin section images. Sorting of massive bedded intervals is better than that of laminar- and cross-bedded, the overall grain size is smaller within massive bedded intervals as well as being less variable in range, and secondary depositional minerals such as potassium feldspar are less prevalent.

4.2.2. NMR-T_2 distribution

T_2 distribution of selected samples that represent CB and MS facies groups are shown in Fig. 5. The NMR-T_2 spectra of cross-bedded plugs (shown in Fig. 5A) show the triple- and quadrimodal distributions for the MH6 and MH7 samples, respectively. T_2 values of the rightmost peak ($T_{2,rmp}$) that corresponds to the dominant pore spaces are 204 and 508 ms, respectively. The micropores, which are usually poorly connected, correspond to the short relaxation time components. The complexity of the bedding structures in the eolian deposition resulted from heterogeneities from pore to sub-core scales. First, grain sizes of the dune sandstone are larger in comparison to those in the ripple sand sheet, leading to larger pore sizes. Further mechanical compaction and pressure solution could further result in smaller T_2 for micro-, meso- and macropores. Second, with respect to the pore-scale heterogeneity, an important influencing factor at sub-core scale is dolomite cement. Cement content at the high permeability layers is much smaller than that of the lower permeability layers. The larger peaks are contributed by the pore spaces from the higher permeability layers, while the middle peak correspond to the pore spaces mainly from the lower permeability layers. Consequently, compared to MH7, the smaller grain size and larger dolomite content contribute to the disappearance of the rightmost peak observed in sample MH6.

The NMR T_2 spectra of massive plugs show the triple-modal distributions, shown in Fig. 5B. The "disordered" packing in massive sandstone with minor changes in the ordering of the individual grains results in wider range of pore types in comparison with those in the cross-bedded samples. Furthermore, pink

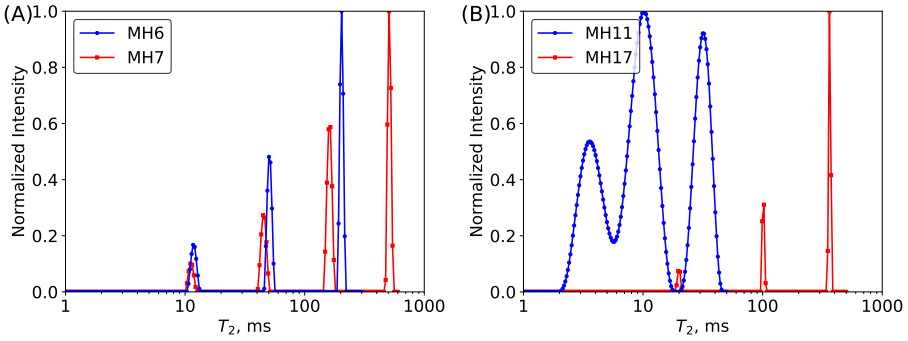

Fig. 5. T_2 distributions of the cross-bedded (MH6 and MH7) and massive (MH11 and MH17) samples. Sample MH7 shows the quadrimodal distribution due to complex pore structure, while MH6 shows the triple-modal distribution because of high dolomite cement content. Massive samples show the triple-modal distributions. The pore-filling dolomite cement in the larger pores left-shift the distribution for MH11.

to gray dolomitic cement together with finer carbonate stringers leads to the smaller pore type, which corresponds to the leftmost peak in the T_2 distribution. In comparison with the sample MH17, sample MH11 has the very fine grains and higher microcrystalline dolomite cement, which result in the triple-modal distribution and smaller T_2. In addition, the number of the pores corresponding to the middle peak is larger than that of the rightmost peak. The pore-filling dolomite cement reduces the size of the larger pores, directly increasing the population of the micropores.

4.2.3. MICP

Pore-throat size distributions (PTSD), shown in Fig. 6, were derived from MICP curves using Equation 1. Pores are assumed cylindrical. The PTSD of the massive sample is uni-modal with the peak at 8.1 μm. Even though the size of the dominant pore spaces is uniform, the wide distribution indicates the existence of smaller pores. In contrast, the high- and low-permeability layers of the cross-bedded sample show a bi-modal characteristic, while the mixture shows a triple-modal characteristic, indicating the complexity of their pore structures. It is interesting to notice that for both massive and mixture samples, the number of the peaks from PTSD is different from that of T_2 distributions. The different characteristics have been reported in previous studies and can be attributed to

several causes (Wang et al., 2018; Wu et al., 2019). First, due to the heterogeneity, the amount of rock pieces used in the MICP experiment cannot fully represent core plug used for T_2 measurement. Secondly, based on Equation 1, MICP measures the pore-throat size (i.e. pore entry radii) and cannot fully represent the size of the pore body, while NMR T_2 estimates both the pore body and throat sizes.

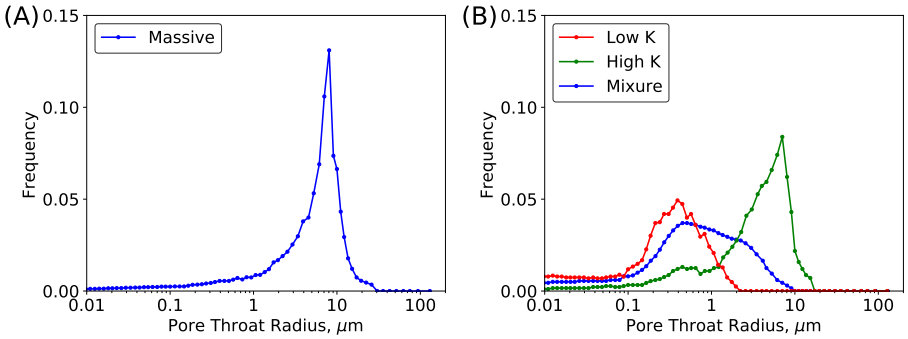

Fig. 6. Pore-throat size distributions of the cross-bedded and massive samples calculated from MICP curves. The samples for the massive and cross-bedded layers were collected close to samples MH17 and MH6. For the cross-bedded layers, the high, low permeability zones, and their mixtures were collected.

4.3. Petrophysical properties characterization

4.3.1. Laboratory porosity and permeability

Cross-plots of nitrogen porosity and permeability are shown in Fig. 7. The massive and cross-bedded facies groups have average porosity and permeability of 0.067 and 3.724 mD, and 0.085 and 16.5 mD, respectively. The coefficients of determination (R^2) of the exponential relations are 0.94 and 0.76 for the massive and cross-bedded facies groups, respectively. Moreover, Fig. 7 shows that porosity and permeability of the CB facies group have a large overlap with that of the the MS facies group, and the former group possesses higher porosity and permeability. This is because petrophysical characteristics of the eolian sandstones are a function of dynamic depositional environment, lithofacies variations and digenetic processes.

In the well UWPRB#1, an excellent zone with high porosity and permeability occurs at the top of the Minnelusa B sandstone, which is largely composed of massive sandstone, such as the reworking of the avalanche dune front. In contrast, for massive sandstone deposited at tubular conditions, cements, like mottled or banding dolomitic carbonate and carbonate mud stringers result in the low porosity and permeability.

For the cross-bedded facies group, higher porosity and permeability for grainflow (or avalanche) deposits, but low angle and planar interdune deposits, i.e., wadi, ripple and grainfall deposits, have low porosity and permeability because of cementation or very fine to fine grain packing. For example, the ripple sandstones were well cemented soon after deposition. In addition, digenetic processes such as cementation, pressure solution, mineral dissolution, and authigenic mineral nucleation can influence the quality of the rocks for both facies groups, which is clearly shown from the SEM and thin section images in Fig. 4. The SEM image shown in Fig. 4B illustrates the relationship between authigenic rhombohedral dolomite grains and larger detrital grains, as well as the in-fill of primary porosity by cements. Figs. 4D and E indicate that cementation is among the most important porosity-reducing diagenetic process. These pore-scale reducing effect not only directly reduces porosity, but also permeability.

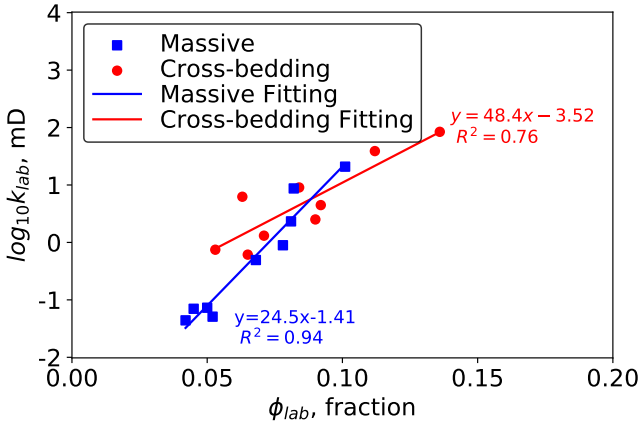

Fig. 7. Nitrogen porosity and permeability of the massive and cross-bedded facies groups in the Minnelusa sandstones. The R^2 are 0.94 and 0.76 for the massive and cross-bedded facies groups, respectively.

In addition to the laboratory measurements, permeability was also estimated from the NMR relaxation data using the SDR and TC models, listed in Table 2. The laboratory and estimated permeability correlate well (Fig. 8). Coefficients C_1 and C_2 are 5.40/8.79 and 1.60E-5/8.94E-4 for the MS/CB facies groups. To evaluate the accuracy of permeability estimated from the NMR relaxation data, the Pearson correlation coefficients (r) between the laboratory and NMR approach for the MS and the CB facies groups were calculated, which are 0.93/0.95 for the SDR model, and 0.93/0.79 for the TC model, respectively. The good correlations indicate the advantage of permeability estimation using the NMR techniques.

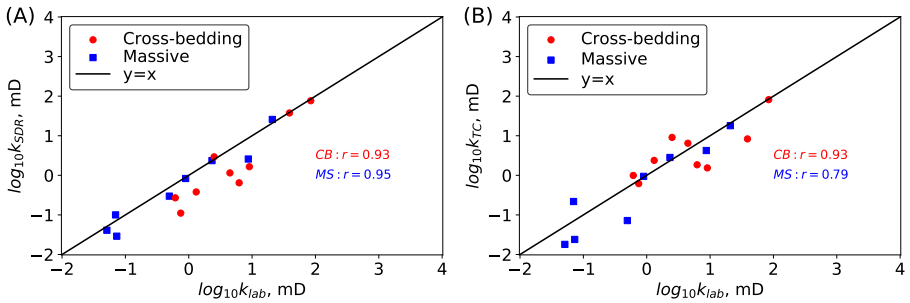

Fig. 8. Cross-plot of (A): k_{lab} vs. k_{SDR}, and (B): k_{lab} vs. k_{TC}. The empirical coefficient C_1 and C_2 are 5.40/8.79 and 1.60E-5/8.94E-4 for the massive and cross-bedded facies groups, respectively.

4.3.2. Porosity and permeability from well-log interpretation

Porosity along the wellbore was obtained directly from the CMR log based on the coefficients C_1 and C_2 obtained from the previous section. Permeability was estimated through the SDR and TC models. In addition, porosity was interpreted by the MLR approach. The fitting parameters, a_0 to a_3, for the cross-bedded and massive groups for the MLR approach are -1.08/0.34/-0.19/0.0049 and 2.20/-0.73/-2257.00/-0.0041, respectively. Then permeability was calculated based on the relationships with porosity shown in Fig. 7.

Fig. 9 shows porosity and permeability results from laboratory measurement, CMR log and MLR approaches. Porosity and permeability interpreted

from CMR log show that high porosity and permeability zones are found in the Minnelusa B Sandstone and the cross-bedded facies zones of the Minnelusa C Sandstone. While for the massive facies zones in the Minnelusa C Sandstone, the formation quality is low. In addition, the variation in vertical direction suggests that the C Sandstone is more heterogeneous. Even though the Minnelusa D Sandstone is thin (17 ft), the relatively high porosity and permeability values could make it a storage zone. It is worth noticing the values of porosity and permeability obtained from the MLR approach at the top of Minnelusa B Sandstone are lower than those estimated by the other two methods(well-log based). This is the result of extrapolation without proper laboratory measurement constraints, missing at the top of the interval. This illustrates the disadvantage of MLR approach, which depends on the laboratory measurements and their coverage along the well-log depth.

4.3.3. Irreducible water saturation

In contrast to oil/gas reservoirs, CO_2 injectivity, storage capacity and migration are three key factors for commercial GCS projects. That means not only high enough porosity and permeability, but a lower irreducible water saturation is desirable. Irreducible water (S_{wir}) is defined as the fraction of water that remains trapped after displacement with a nonwetting phase (Morrow, 1970). In general, higher clay-bound water is a direct consequence of higher clay volume fraction, and a higher capillary bound water saturation indicates complex pore geometry and networks, which results from cementation.

NMR-T_2 spectrum directly reflects the pore size distribution in fully saturated rock. Herein, an empirical T_2 cut-off value of 33 ms was used to split the T_2 spectrum into bound water (<33 ms) and free water (>33 ms). Fig. 10 shows S_{wir} histograms calculated from CMR T_2 spectra of the two facies groups. The irreducible water saturation varies from 0.0 to 0.8, with an average of 0.27 and 0.15 for the MS and CB facies groups, respectively. In this study, larger content of the dolomite cements, which might produce tight porosity similar to that related to clays, for the massive facies group might result in larger irre-

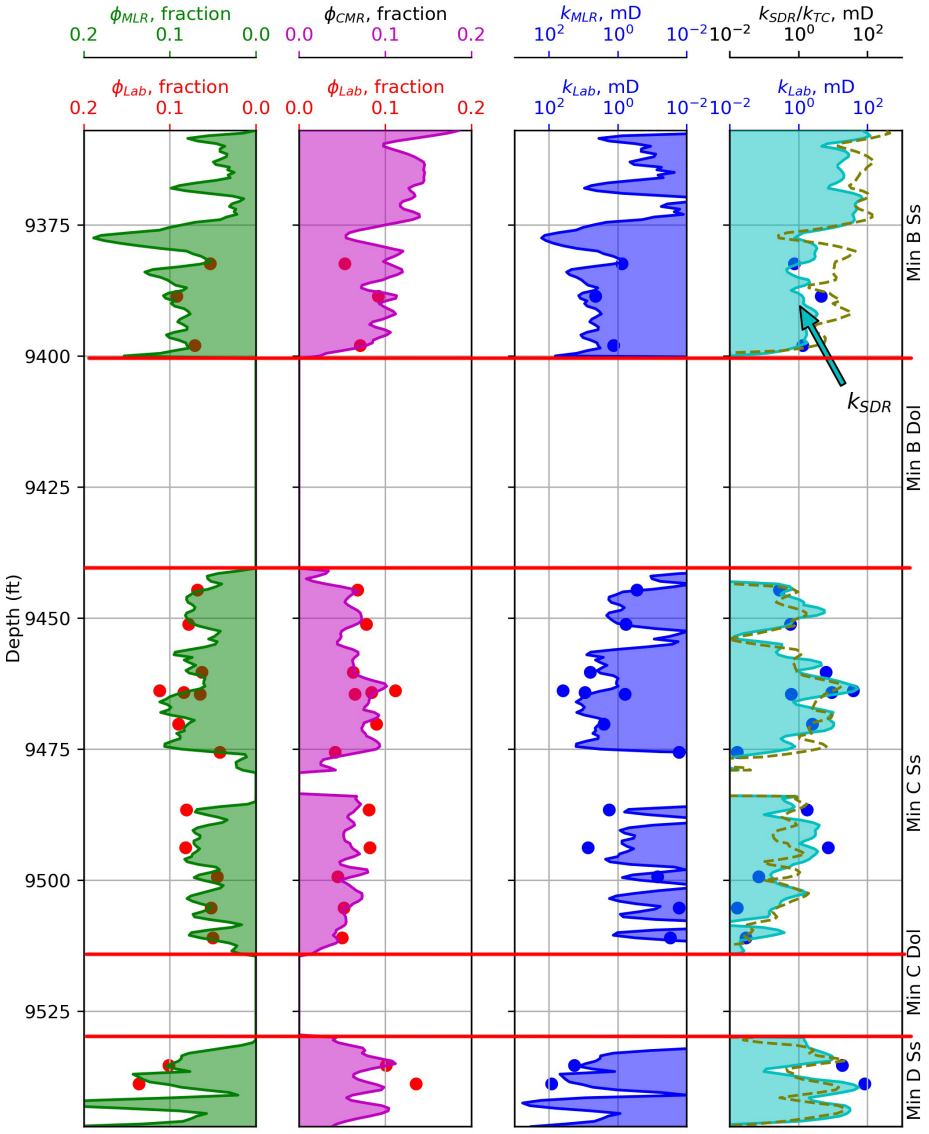

Fig. 9. Log and laboratory (dots) porosity and permeability results. High porosity and permeability zones are found in the Minnelusa B Sandstone and the cross-bedded facies zones of the Minnelusa C Sandstone. For the MLR approach, abnormal higher or lower values of porosity and permeability are observed. On the fourth track, K_{SDR} curve is the solid line with filling color, as annotated by the arrow. Min: Minnelusa, Ss: Sandstone, Dol: Dolostone.

ducible water saturation. In addition, the by-pass effect due to high seepage resistance (high capillary pressure) dominates locally as the heterogeneity of pore structures mainly exits at the pore level, while at the core-scale, the irreducible water saturation might be homogeneously distributed for the massive facies group. In contrast, for the cross-bedded facies group, the by-pass effect is pronounced at the core level because of the lower permeability zones, from where the bound water volume mainly comes. While for the higher permeability zones, which possess the most pore spaces, the irreducible water saturation is mainly controlled by the pore-level by-pass effect.

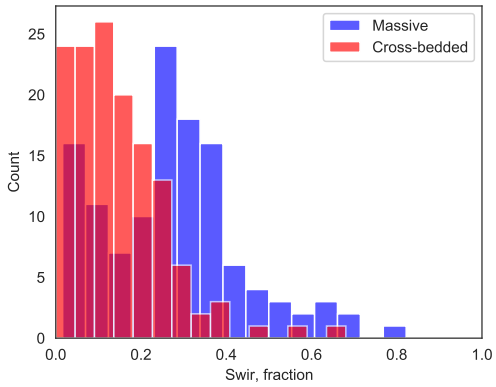

Fig. 10. Histograms of S_{wir} of the massive and cross-bedded facies groups calculated from CMR log. An empirical T_2 cut-off value of 33 ms was employed to partition the T_2 spectrum into bound water (<33 ms) and free water (>33 ms). The irreducible water saturation varies from 0.0 to 0.8, with an average of 0.27 and 0.15 for the MS and CB facies groups, respectively.

To further investigate the dominant influencing factors on S_{wir}, the relationships between S_{wir} with ϕ_{CMR} and T_{2LM} are depicted in Fig. 11. Fig. 11A shows that the irreducible water saturation decreases with the increase of porosity. However, the negative correlation is weak for both facies groups indicating that porosity has less impact on S_{wir} for both facies groups. S_{wir} is also inversely proportional to T_{2LM}, as shown in Fig. 11B. The relative good trends denoted by the values of R^2, which are weakly correlated to porosity, indicate that the irreducible water saturation is mainly related to the rock type (different correlations for different types, and consequently controlled by pore structure.

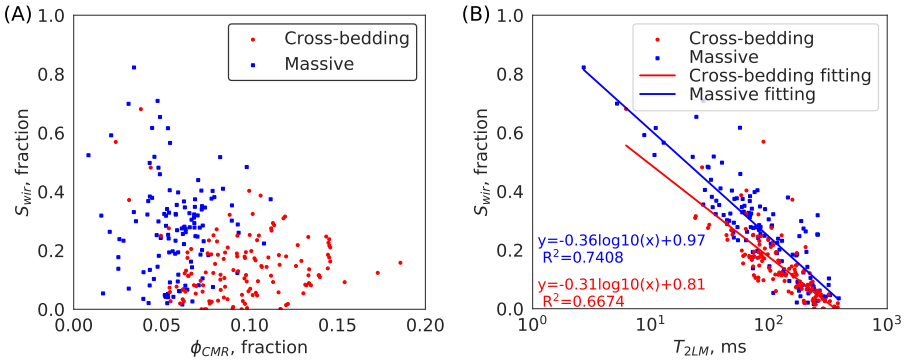

Fig. 11. (A) Relationships of ϕ_{wir} vs S_{wir}, and (B) T_{2LM} vs S_{wir}. S_{wir} was calculated from CMR T_2 spectra using the empirical T_2 cut-off value of 33 ms. For T_{2LM} vs S_{wir}, R^2 of the massive and cross-bedded facies groups are 0.74 and 0.67, respectively.

4.4. Flow unit classification

Fig. 12 shows that the high quality intervals are mainly located in the cross-bedded facies group of the Minnelusa B, C and D sands, indicating that the main CO_2 flow zones would occur in these intervals. For the massive facies group, the overall poor quality would result in lower CO_2 injectivity and storage capacity.

Four DRT units (11, 12, 13, and 14) were subdivided, shown in Fig. 12. The flow units 13 and 14 exhibit good reservoir quality with favorable porosity and permeability, and smaller irreducible water saturation (Fig. 13). In contrast, flow units 11 and 12 are not favorable to CO_2 flow capacity due to lower porosity and permeability, and larger irreducible water saturation. Fig. 13 depicts the thickness of different flow units for both groups and the cross-plots of their corresponding porosity and permeability, respectively. The total thickness of the flow units 13 and 14 for the cross-bedded facies group is 87 ft with 50 ft of good quality flow unit 14. For the massive facies group, the total thickness of the flow units 13 and 14 is 69 ft with only 30 ft for flow unit 4, and the thickness of flow unit 2 is up to 46 ft.

In addition to the quality of the flow units, their continuity and variation along the well depth also play an important role in the CO_2 injectivity and its profile. Examination of the flow units in Minnelusa B and D Sandstones shows that these units are less variable, implying that the CO_2 injectivity profile is

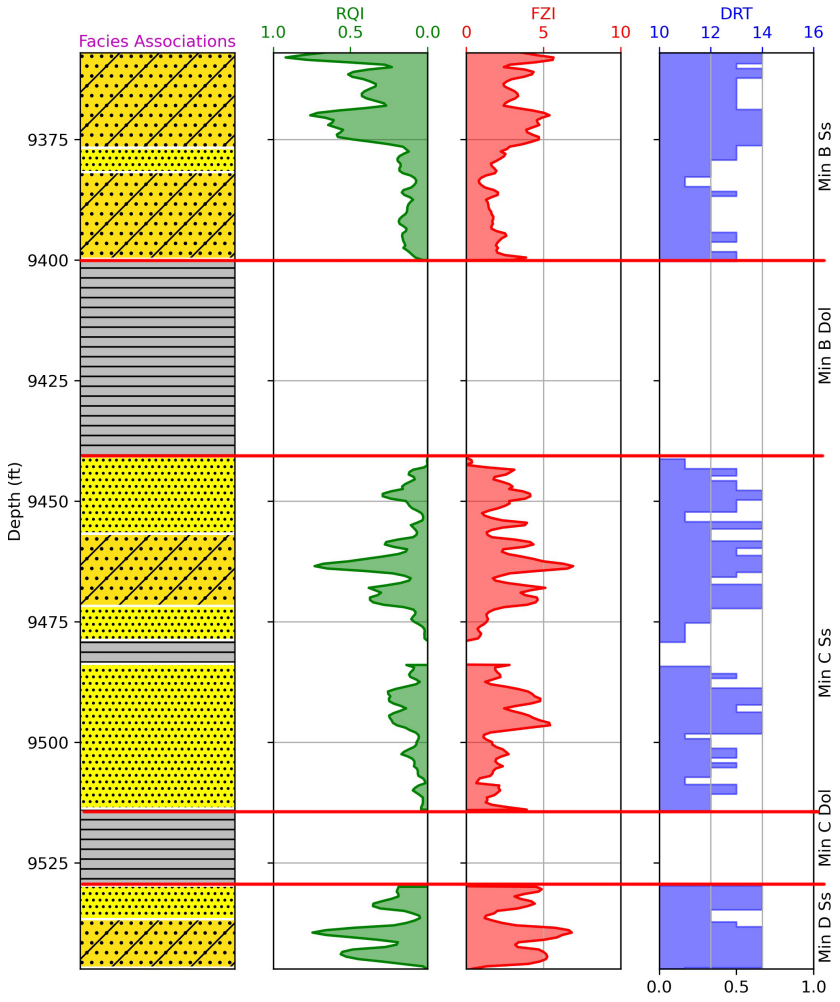

Fig. 12. Reservoir quality index, flow zone indicator and discrete rock types for the two facies groups. Four flow units (DRT = 11, 12, 13, and 14) were subdivided for both facies groups. Flow units along the well depth are more continuous and uniform for both facies group in Minnelusa B and D sands, while more heterogeneous in Minnelusa C sand.

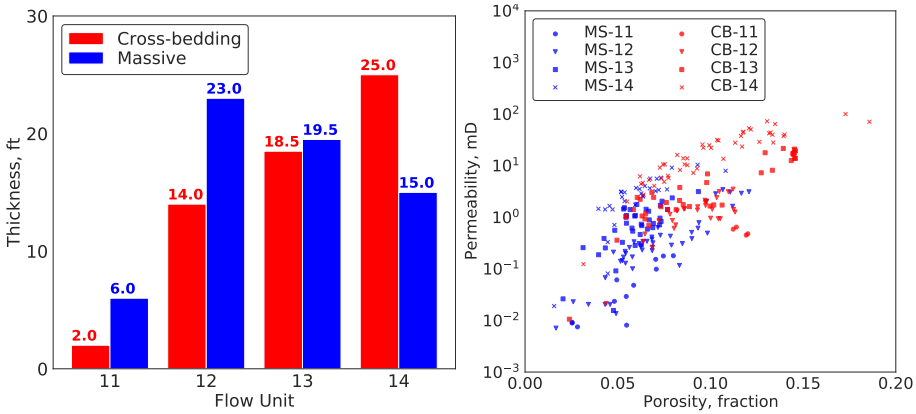

Fig. 13. Left: Thickness of the flow units for the MS and CB facies groups. Right: Cross-plots of porosity and permeability obtained from CMR log for the flow units of the two facies groups. The overall reservoir quality for the CB facies group is better and the thickness of the good quality intervals (DRT=14) are larger than the MS facies group.

more homogeneous. Flow units in the C Sandstone vary within a short distance, which should lead to more heterogeneous CO_2 injectivity profile. Even though the tight zones can act as barriers to hinder the migration of CO_2 in the vertical direction, they would also cause CO_2 fingering through high permeability zones, which would lead to a lower sweep efficiency. Thus the CO_2 storage capacity would be reduced and the CO_2 plume size would be enlarged.

5. Conclusions and implications for GCS in eolian reservoirs

In this paper, the multiscale petrophysical characterization was performed for the Minnelusa B, C and D Sandstones to evaluate geological carbon storage. While geological compelxity is inherent to these eolian systems, the research results in this work led to the classification of the two main facies groups, massive and cross-bedded, through identification of depositional features. For the massive facies group, the interdune strata show massive grain packing, and the reservoir quality is mainly controlled by diagenetic effects. The cross-bedded facies group is characterized as pore- to core-scale cross- or laminar-bedded sandstones. Depositional environments and dolomite cement content are the two dominant influencing factors on reservoir qualities. Furthermore, labora-

tory T_2 distributions and MICP show the complex pore structure for the CB facies group, while for the MS facies, pore (throat) size are broader and more uniform. Routine porosity and permeability measurements of both facies groups show good relationships. Permeability estimated by the SDR and the TC models using laboratory T_2 distribution and CMR logging data, and porosity obtained from the CMR log show good correlation with experimental measurements, indicating the advantage of the NMR techniques in petrophysical characterization of eolian reservoirs compared to conventional well logs.

By employing the classified facies groups, and effective porosity and permeability interpreted from CMR log, four discrete rock types were determined for the two facies groups. Moreover, the value of the classification method can be additionally appreciated by trends of irreducible water saturation that strongly correlate to the classified rock groups. This is an indication of the internal consistency of our classification method. The thicknesses of the flow units 13 and 14 for the cross-bedded facies groups are larger than that of the massive, designating it as the high potential CO_2 injection zones. The results can be used as the primary data to predict the flow unit variation across the area of interest and as the input data for 3D geological modeling and CO_2 injection simulation.

The findings in this study have broader implications for not only geological carbon storage, but also CO_2 enhanced oil recovery in eolian reservoirs. Furthermore, results will also help to understand pore- to log-scale reservoir characteristics. Models involving grain parameters may not be adequate to appropriately predict permeability within an eolian reservoir because higher and lower permeability eolian facies do not always have resolvable porosity differences. The appropriate flow units partitioning of eolian reservoirs should be performed based on the geological facies characterization and classification. Even though CO_2 injectivity for the good units of CB facies group is more suitable for GCS than the MS facies group in view of the reservoir quality and thickness, CO_2 storage capacity and migration in the CB facies group is worse due to the multi-scale heterogeneities and lower volumetric sweep efficiency (Kou et al., 2021). In addition, as less data are available in the study area, the lateral

continuity also increases the uncertainty of the commercialization of the GCS. Further exploration, including drilling a new test well, conducting a 3D seismic survey, performing cross-well interference test are proposed in Phase III of the project.

Acknowledgments

The authors thank the Department of Energy for funding through the grants DE-FE0031624. This manuscript is the result of work sponsored by an agency of the United States Government. Neither the United States Government nor any agency thereof, nor any of their employees, makes any warranty, express or implied, or assumes any legal liability or responsibility for the accuracy, completeness, or usefulness of any information, apparatus, product, or process disclosed, or represents that its use would not infringe privately owned rights. Reference herein to any specific commercial product, process, or service by trade name, trademark, manufacturer, or otherwise does not necessarily constitute or imply its endorsement, recommendation, or favoring by the United States Government or any agency thereof. The views and opinions of authors expressed herein do not necessarily state or reflect those of the United States Government or any agency thereof. The authors thank Tao Bai for core plug preparation.

References

Al-Bayati, D., Saeedi, A., Myers, M., White, C., Xie, Q., 2019. An experimental investigation of immiscible-CO_2-flooding efficiency in sandstone reservoirs: Influence of permeability heterogeneity. SPE Reservoir Evaluation & Engineering 22, 990–997. doi:https://doi.org/10.2118/190876-PA.

Alvarado, R.J., Damgaard, A., Hansen, P., Raven, M., Heidler, R., Hoshun, R., Kovats, J., Morriss, C., Rose, D., Wendt, W., 2003. Nuclear magnetic resonance logging while drilling. Oilfield Rev 15, 40–51. doi:https://doi.org/10.2118/105605-MS.

Amaefule, J.O., Altunbay, M., Tiab, D., Kersey, D.G., Keelan, D.K., 1993. Enhanced reservoir description: Using core and log data to identify hydraulic (flow) units and predict permeability in uncored intervals/wells. doi:10.2118/26436-MS. SPE-26436-MS.

Anna, O., 2009. Geologic assessment of undiscovered oil and gas in the Powder River Basin province. Wyoming and Montana: US Geological Survey Digital Data Series DDS-69-U .

Chandler, M.A., Kocurek, G., Goggin, D.J., Lake, L.W., 1989. Effects of stratigraphic heterogeneity on permeability in eolian sandstone sequence, Page Sandstone, northern Arizona. AAPG Bulletin 73, 658–668. doi:https://doi.org/10.1306/44B4A249-170A-11D7-8645000102C1865D.

Chandra, V., Barnett, A., Corbett, P., Geiger, S., Wright, P., Steele, R., Milroy, P., 2015. Effective integration of reservoir rock-typing and simulation using near-wellbore upscaling. Marine and Petroleum Geology 67, 307–326. doi:https://doi.org/10.1016/j.marpetgeo.2015.05.005.

Chen, M., Al-Maktoumi, A., Rajabi, M.M., Izady, A., Al-Mamari, H., Cai, J., 2021. Evaluation of CO_2 sequestration and circulation in fault-bounded thin geothermal reservoirs in North Oman using response surface methods. Journal of Hydrology 598, 126411. doi:https://doi.org/10.1016/j.jhydrol.2021.126411.

Coates, G., Peveraro, R., Hardwick, A., Roberts, D., 1991. The magnetic resonance imaging log characterized by comparison with petrophysical properties and laboratory core data, in: SPE Annual Technical Conference and Exhibition, Society of Petroleum Engineers. pp. 627–635. doi:https://doi.org/10.2118/22723-MS.

Coates, G.R., Xiao, L., Prammer, M.G., 1999. NMR logging: principles and applications. volume 234. Haliburton Energy Services Houston.

Farshi, M., Moussavi-Harami, R., Mahboubi, A., Khanehbad, M., Golafshani, T., 2019. Reservoir rock typing using integrating geological and petrophysical properties for the Asmari Formation in the Gachsaran oil field, Zagros basin. Journal of Petroleum Science and Engineering 176, 161–171. doi:https://doi.org/10.1016/j.petrol.2018.12.068.

Fryberger, S.G., 1984. The Permian Upper Minnelusa Formation, Wyoming: Ancient example of an offshore-prograding eolian sand sea with geomorphic facies, and system-boundary traps for petroleum, in: 35th Annual Field Conference Guidebook, Wyoming Geological Association. pp. 241–271.

George, G.R., 1984. Cyclic sedimentation and depositional environments of the Upper Minnelusa Formation, central Campbell County, Wyoming: Wyoming Geological Association , 75–95.

Godec, M., Koperna, G., Petrusak, R., Oudinot, A., 2013. Potential for enhanced gas recovery and CO_2 storage in the Marcellus Shale in the Eastern United States. International Journal of Coal Geology 118, 95–104. doi:https://doi.org/10.1016/j.coal.2013.05.007.

Gong, Y., Gu, Y., 2015. Miscible CO_2 simultaneous water-and-gas (CO_2-SWAG) injection in the Bakken formation, in: SPE/CSUR Unconventional Resources Conference, OnePetro. doi:https://doi.org/10.2118/175976-MS.

Gunter, G., Finneran, J., Hartmann, D., Miller, J., 1997. Early determination of reservoir flow units using an integrated petrophysical method, in: SPE Annual Technical Conference and Exhibition, Society of Petroleum Engineers. pp. 373–380. doi:https://doi.org/10.2118/38679-MS.

Guo, G., Diaz, M.A., Paz, F.J., Smalley, J., Waninger, E.A., 2007. Rock typing as an effective tool for permeability and water-saturation modeling: A case study in a clastic reservoir in the oriente basin. SPE Reservoir Evaluation & Engineering 10, 730–739. doi:https://doi.org/10.2118/97033-PA.

Han, G., Han, W.S., Kim, K.Y., Baek, J., Kim, M., Kim, C.Y., Lim, J.H., 2021. Characterizing locality-and Scale-Dependent Heterogeneity in Conglomerate Core and Associated Fluid Flow using X-ray CT imaging. Journal of Hydrology , 126736doi:https://doi.org/10.1016/j.jhydrol.2021.126736.

IPCC, 2013. Climate change 2013: The physical science basis. Contribution of working group I to the fifth assessment report of the Intergovernmental Panel on Climate Change 1535.

Jiang, L., Chen, Z., Ali, S.F., 2019. Feasibility of carbon dioxide storage in post-burn underground coal gasification cavities. Applied Energy 252, 113479. doi:https://doi.org/10.1016/j.apenergy.2019.113479.

Jorgensen, S.D., James, S.W., 1988. Integration of stratigraphic high resolution dipmeter data into the development of the Minnelusa, in: 39th Annual Field Conference Guidebook, Wyoming Geological Association. pp. 105–116.

Kenyon, W., 1992. Nuclear magnetic resonance as a petrophysical measurement. Nuclear Geophysics 6, 153–171.

Kenyon, W., 1997. Petrophysical principles of applications of NMR logging. The Log Analyst 38.

Kenyon, W., Day, P., Straley, C., Willemsen, J., 1988. A three-part study of NMR longitudinal relaxation properties of water-saturated sandstones. SPE Formation Evaluation 3, 622–636. doi:https://doi.org/10.2118/15643-PA.

Kou, Z., Wang, H., Alvarado, V., McLaughlin, J.F., Quillinan, S.A., 2021. Impact of sub-core scale heterogeneity on CO_2/brine multiphase flow for geological carbon storage in the upper Minnelusa sandstones. Journal of Hydrology 599, 126481. doi:https://doi.org/10.1016/j.jhydrol.2021.126481.

Krevor, S.C., Pini, R., Li, B., Benson, S.M., 2011. Capillary heterogeneity trapping of CO_2 in a sandstone rock at reservoir conditions. Geophysical Research Letters 38. doi:https://doi.org/10.1029/2011GL048239.

Krystinik, L., 1990. Diagenesis in ancient eolian sandstone, in: Modern and Ancient Eolian Deposits: Petroleum Exploration and Production, Rocky Mountain Section (SEPM). pp. 147–160.

Leverett, M., 1941. Capillary behavior in porous solids. Transactions of the AIME 142, 152–169. doi:https://doi.org/10.2118/941152-G.

Liu, Y., Iglauer, S., Cai, J., Amooie, M.A., Qin, C., 2019. Local instabilities during capillary-dominated immiscible displacement in porous media. Capillarity 2, 1–7. doi:10.26804/capi.2019.01.01.

Morrow, N.R., 1970. Irreducible wetting-phase saturations in porous media. Chemical Engineering Science 25, 1799–1815. doi:https://doi.org/10.1016/0009-2509(70)80070-7.

Newell, A.J., Pourmalek, A., Butcher, A.S., Shariatipour, S.M., 2019. The importance of lithofacies control on fluid migration in heterogeneous aeolian formations for geological CO_2 storage: Lessons from observational evidence and modelling of bleached palaeoreservoirs at Salt Wash Graben, Utah. International Journal of Greenhouse Gas Control 91, 102841. doi:https://doi.org/10.1016/j.ijggc.2019.102841.

Padhi, A., Mallick, S., Behzadi, H., Alvarado, V., 2014. Efficient modeling of seismic signature of patchy saturation for time lapse monitoring of carbon sequestrated deep saline reservoirs. Applied Energy 114, 445–455. doi:https://doi.org/10.1190/1.3627664.

Pittman, E.D., 1992. Relationship of porosity and permeability to various parameters derived from mercury injection-capillary pressure curves for sandstone. AAPG Bulletin 76, 191–198. doi:https://doi.org/10.1306/BDFF87A4-1718-11D7-8645000102C1865D.

Rebelle, M., Lalanne, B., 2014. Rock-typing in carbonates: A critical review of clustering methods, in: Abu Dhabi International Petroleum Exhibition

747 and Conference, Society of Petroleum Engineers. doi:https://doi.org/10.
748 2118/171759-MS.

749 Rebelle, M., Umbhauer, F., Poli, E., 2009. Pore to grid carbonate rock-typing,
750 in: IPTC International Petroleum Technology Conference. doi:10.2523/
751 IPTC-13120-MS. IPTC-13120-MS.

752 Ren, S., Parsekian, A.D., Zhang, Y., Carr, B.J., 2019. Hydraulic conductivity
753 calibration of logging NMR in a granite aquifer, Laramie Range, Wyoming.
754 Groundwater 57, 303–319. doi:10.1111/gwat.12798.

755 Saghafi, A., Faiz, M., Roberts, D., 2007. CO_2 storage and gas diffusivity prop-
756 erties of coals from Sydney Basin, Australia. International Journal of Coal
757 Geology 70, 240–254. doi:https://doi.org/10.1016/j.coal.2006.03.006.

758 Salman, S.M., Bellah, S., 2009. Rock typing: An integrated reservoir char-
759 acterization tool to construct a robust geological model in Abu Dhabi car-
760 bonate oil field, in: SPE/EAGE Reservoir Characterization & Simulation
761 Conference, European Association of Geoscientists & Engineers. pp. cp–170.
762 doi:https://doi.org/10.2118/125498-MS.

763 Schenk, C., 1990. Overview of eolian sandstone diagenesis, permian upper part
764 of the Minnelusa Formation, Powder River Basin, Wyoming, in: Modern
765 and Ancient Eolian Deposits: Petroleum Exploration and Production, Rocky
766 Mountain Section (SEPM). pp. 223–234.

767 Shurr, G.W., Ludvigson, G.A., Hammond, R.H., 1994. Perspectives on the east-
768 ern margin of the Cretaceous Western Interior Basin. volume 287. Geological
769 Society of America. doi:https://doi.org/10.1130/SPE287.

770 Singh, H., 2018. Impact of four different CO_2 injection schemes on extent of
771 reservoir pressure and saturation. Advances in Geo-Energy Research 2, 305–
772 318. doi:10.26804/ager.2018.03.08.

773 Skalinski, M., Kenter, J.A., 2015. Carbonate petrophysical rock typing: Inte-
774 grating geological attributes and petrophysical properties while linking with

dynamic behaviour. Geological Society, London, Special Publications 406, 229–259. doi:https://doi.org/10.1144/SP406.6.

U.S. Energy Information Administration, 2020. State energy profiles: Wyoming. https://www.eia.gov/beta/states/states/wy/overview. Accessed: 2020-06-30.

Wang, H., Alvarado, V., McLaughlin, J.F., Bagdonas, D.A., Kaszuba, J.P., Campbell, E., Grana, D., 2018. Low-field nuclear magnetic resonance characterization of carbonate and sandstone reservoirs from rock spring uplift of Wyoming. Journal of Geophysical Research: Solid Earth 123, 7444–7460. doi:10.1029/2018JB015779.

Wei, N., Gill, M., Crandall, D., McIntyre, D., Wang, Y., Bruner, K., Li, X., Bromhal, G., 2014. CO_2 flooding properties of Liujiagou sandstone: Influence of sub-core scale structure heterogeneity. Greenhouse Gases: Science and Technology 4, 400–418. doi:10.1002/GHG.1407.

Wu, Y., Tahmasebi, P., Lin, C., Zahid, M.A., Dong, C., Golab, A.N., Ren, L., 2019. A comprehensive study on geometric, topological and fractal characterizations of pore systems in low-permeability reservoirs based on SEM, MICP, NMR, and X-ray CT experiments. Marine and Petroleum Geology 103, 12–28. doi:https://doi.org/10.1016/j.marpetgeo.2019.02.003.

Yu, Y., Yang, G., Cheng, F., Yang, S., 2021. Effects of impurities N_2 and O_2 on CO_2 storage efficiency and costs in deep saline aquifers. Journal of Hydrology 597, 126187. doi:https://doi.org/10.1016/j.jhydrol.2021.126187.

Zhang, L., Wang, Y., Miao, X., Gan, M., Li, X., 2019. Geochemistry in geologic CO_2 utilization and storage: A brief review. Advances in Geo-Energy Research 3, 304–313. doi:10.26804/ager.2019.03.08.

Zheng, T., Guo, B., Shao, H., 2021. A hybrid multiscale framework coupling multilayer dynamic reconstruction and full-dimensional models for CO_2 stor-

age in deep saline aquifers. Journal of Hydrology 600, 126649. doi:https://doi.org/10.1016/j.jhydrol.2021.126649.